Transport upscaling in highly heterogeneous aquifers and the prediction of tracer dispersion at the Macrodispersion Experiment (MADE) site

Marco Dentz[1], Alessandro Comolli[1], Vivien Hakoun[2], and Juan Hidalgo[1]

[1]IDAEA-CSIC
[2]BRGM, University of Montpellier

November 26, 2022

Abstract

We present an upscaled Lagrangian approach to predict the plume evolution in highly heterogeneous aquifers. The model is parameterized by transport independent characteristics such as the statistics of hydraulic conductivity and the Eulerian flow speed. It can be conditioned on the tracer properties, the conductivity data at the injection region, and is able to account for mobile-immobile mass transfer. Thus, the model is transferable to different solutes and hydraulic conditions. It captures the large scale non-Gaussian features for the evolution of the longitudinal mass distribution observed for the bromide and tritium tracer plumes at the macrodispersion experiment (MADE) site (Columbus, Ohio, USA), which are characterized by a slow moving peak and pronounced forward tailing. These large scale features are explained by advective tracer propagation due to a broad distribution of spatially persistent Eulerian flow speeds as a result of spatial variability in hydraulic conductivity.

1

Transport upscaling in highly heterogeneous aquifers and the prediction of tracer dispersion at the Macrodispersion Experiment (MADE) site

Marco Dentz[1], Alessandro Comolli[1,2], Vivien Hakoun[1,3], and Juan Hidalgo[1]

[1]*Spanish National Research Council (IDAEA-CSIC), Barcelona, Spain**

[2]*Université Libre de Bruxelles (ULB), Nonlinear Physical Chemistry Unit, CP 231, 1050, Bruxelles, Belgium and*

[3]*BRGM, University of Montpellier, Montpellier, 34000, France*

We present an upscaled Lagrangian approach to predict the plume evolution in highly heterogeneous aquifers. The model is parameterized by transport independent characteristics such as the statistics of hydraulic conductivity and the Eulerian flow speed. It can be conditioned on the tracer properties, the conductivity data at the injection region, and is able to account for mobile-immobile mass transfer. Thus, the model is transferable to different solutes and hydraulic conditions. It captures the large scale non-Gaussian features for the evolution of the longitudinal mass distribution observed for the bromide and tritium tracer plumes at the macrodispersion experiment (MADE) site (Columbus, Ohio, USA), which are characterized by a slow moving peak and pronounced forward tailing. These large scale features are explained by advective tracer propagation due to a broad distribution of spatially persistent Eulerian flow speeds as a result of spatial variability in hydraulic conductivity.

I. INTRODUCTION

The upscaling and prediction of tracer transport in highly heterogeneous porous and fractured media is of central concern in a broad range of subsurface applications from groundwater management to underground gas and waste storage. This task is challenging due to strong spatial variability in hydraulic conductivity values encountered in geological media [1].

Spatial variability in hydraulic conductivity induces spatial fluctuations in the flow and transport velocities, whose impact on large scale tracer migration has been quantified in terms of macrodispersion coefficients [2, 3]. For moderately heterogeneous media, [2] used a stochastic modeling approach [4–6] to express the longitudinal macrodispersion coefficients in terms of the mean flow velocity, and the correlation length and variance of the logarithm of hydraulic conductivity. This expression is a central results for hydrogeological prediction because it allows to forecast macroscopic transport features based on transport independent observables.

However, spatial heterogeneity gives rise to transport behaviors that can be very different from the ones predicted by advection-dispersion models characterized by constant macrodispersion coefficients. For pointlike solute injections, the latter predicts Gaussian shaped tracer plumes and breakthrough curves, while observed distributions are typically found to be non-Gaussian [7–11]. This is the case for the tracer plumes observed during the macrodispersion experiments conducted in the alluvial aquifer underlying the Columbus Air Force Base in northeastern Mississippi [7, 12]. Spatial tracer distributions are characterized by strongly non-Gaussian shapes characterized by a slowly moving peak and a pronounced forward tail. These and other observations of anomalous solute dispersion have spurred the development of non-Fickian transport theories [13–16]. Those include multirate mass transfer approaches [17, 18], continuous time random walks [13, 19], fractional advection-dispersion models [20, 21], time-domain random walks [22, 23], and space-time non-local advection-dispersion equations [24, 25]. While all of these approaches provide dynamic frameworks to model non-Gaussian large scale transport features, their parameterization in terms of transport independent parameters and thus their predictive power remain open questions.

The migration of the tracer plume at the MADE site was modeled by Berkowitz and Scher [26] with the continuous time random walk (CTRW) approach based on an empirical distribution of transition length and times, which reflects a broad distribution of mass transfer time scales. Schumer *et al.* [27] modeled the tracer plumes of the MADE-1 experiment using a fractal mobile-immobile model that accounts for both solute retention due to a broad distribution of mass transfer time scale, and preferential transport due to a broad distribution of mass transfer length scales. The characteristic exponents of the model are estimated from the experimental data. Harvey and Gorelick [28] model the plume evolution using a multirate mass transfer (MRMT) model that considers rate limited mass transfer between a mobile domain with accelerating flow, and an immobile zone, which represents intragranular porosity, low permeability zones, dead end pores and surface sorption sites. These different processes are represented by a capacity coefficient,

---

a rate coefficient, a retardation coefficient, a velocity parameter and an acceleration parameter, which are estimated from the experimental mass data. These modeling approaches propose a range of mass transfer processes and invoke broad distributions of mass transfer time scales and lengths in order to simulate the impact of medium and flow heterogeneity on large scale transport. A key question in order to constrain such models refers to the dominant local scale mechanisms that cause non-Fickian large scale transport.

Mobile-immobile mass transfer has been studied as a mechanism to explain the decay of the apparent solute mass observed at the MADE-1 and MADE-2 experiments [28]. Feehley *et al.* [29] and Guan *et al.* [30] combine a stochastic reconstruction of aquifer heterogeneity based on fractal Brownian motion with mobile-immobile mass transfer in order to assess the plume evolution in the MADE-2 experiment. A series of works [31–33] have shown that a local scale advection-dispersion model based on the detailed knowledge of the spatial distribution of hydraulic conductivity allows reproducing the spatial distribution of tracer plumes observed at the MADE site. This implies that some key features of transport may indeed be understood from the spatial variability of hydraulic conductivity and thus advective heterogeneity. The question arising from this observation is whether characteristics of non-Fickian transport in strongly heterogeneous media can be predicted based only on a few geostatistical medium characteristics similar to the prediction of macrodispersion in moderately heterogeneous media. Along these lines, several authors [23, 34–36] investigated the relation between advective travel times and hydraulic conductivity, and the impact of broad distributions of the logarithm of hydraulic conductivity on non-Fickian transport. For example, the stochastic multi-indicator approach of Fiori *et al.* [23] was adapted in Fiori *et al.* [37] to predict the plume evolution of the MADE-1 experiment based on analytical expressions for the advective travel times over rectangular inclusions.

In this paper, we adress the questions of upscaling and prediction of dispersion in highly heterogeneous aquifers in terms of medium and flow heterogeneity, using transport independent parameters. We use a stochastic time domain random walk approach [38, 39] that accounts for heterogeneous advection and mobile-immobile mass transfer. This approach propagates particles in space and time according to a velocity Markov model that is determined by the distribution of the Eulerian flow speed and correlation length, this means in terms of transport independent quantities. Mobile-immobile mass transfer is modeled using a compound Poisson process [40, 41] We discuss the model and its parameterization in terms of the medium and flow properties, and use it for the modeling and interpretation of the one-dimensional tracer profiles of the MADE-1 experiment.

II.   UPSCALED TRANSPORT MODEL

We employ the stochastic time-domain random walk (TDRW) implementation presented in [39] in order to built an upscaled model to predict the concentration evolution in highly heterogeneous aquifers, based on the statistical characteristics of the logarithm of hydraulic conductivity, the flow speed, porosity and the mean hydraulic gradient. The method quantifies particle motion in spatially variable flow fields through a stochastic model for particle speeds along streamlines. Thus, it propagates solute particles at constant space increments whose duration is obtained from a Markov chain representation for the particle speed. It can be parameterized by transport independent medium and flow characteristics. This approach has been used for the upscaling and prediction of solute transport from the pore to Darcy scale, and from the Darcy to the field scale in two- and three-dimensional porous and fractured media [11, 39, 42–47]. In the following, we detail the model, its assumptions, and parameterization, as well as an extension to account for mobile-immobile mass transfer.

A.   Stochastic advective motion

Purely advective particle motion in a spatially variable hydraulic conductivity field is quantified by the following stochastic evolution equations for the longitudinal particle position $x(s)$ and the advective travel time $t_a(s)$ [39, 48],

$$\frac{dx(s)}{ds} = \chi^{-1}, \qquad\qquad \frac{dt_a(s)}{ds} = \frac{1}{v_\ell(s)} \qquad\qquad (1)$$

where s is the distance along streamline, $v_\ell(s) > 0$ the particle speed and χ advective tortuosity. Advective tortuosity measures the ratio of streamline distance and average linear distance [39]. The particle speed $v_\ell(s)$ describes an ergodic and stationary Markov process characterized by the steady state distribution $p_v(v)$. The latter is a Lagrangian quantity, which, however, can be related to the distribution of Eulerian flow speed $p_e(v)$ via the flux-weighting relation [39, 48]

$$p_v(v) = \frac{v p_e(v)}{\langle v_e \rangle}. \qquad\qquad (2)$$

Note that $v_\ell(s)$ evolves as a function of distance s along a streamline, while in classical Lagrangian methods [4], particle speeds evolve with travel time. This difference explains the flux-weighting relationship (2) as discussed in detail in Dentz *et al.* [48] and Hakoun *et al.* [38].

The Eulerian velocity $\mathbf{v}_e(\mathbf{x})$ is given in terms of the Darcy flux $\mathbf{q}(\mathbf{x})$, porosity ϕ, and the retardation coefficient θ. We assume that both porosity and retardation are constant. The Darcy flux satisfies

$$\mathbf{q}(\mathbf{x}) = -K(\mathbf{x})\nabla h(\mathbf{x}), \qquad\qquad \nabla \cdot \mathbf{q}(\mathbf{x}) = 0, \qquad\qquad (3)$$

where $K(\mathbf{x})$ is hydraulic conductivity and $h(\mathbf{x})$ hydraulic head. The flow problem (3) is solved numerically for a unit mean hydraulic gradient aligned with the coordinate axis in one-direction, and a unit geometric mean conductivity $K_g = 1$, see the supplementary information for details. The Eulerian velocity $\mathbf{v}_e(\mathbf{x})$ is given in terms of the resulting Darcy velocity $\mathbf{q}(\mathbf{x})$ as

$$\mathbf{v}_e(\mathbf{x}) = v_0 \mathbf{q}(\mathbf{x}) \qquad\qquad\qquad v_0 = K_g J/\phi\theta \qquad\qquad (4)$$

where J is the magnitude of the mean hydraulic gradient. The velocity v_0 and the correlation length λ define the characteristic time $\tau_v = \lambda/v_0$. Note that changes in v_0 affect transport only through a rescaling of time. The Eulerian speed is $v_e(\mathbf{x}) = |\mathbf{v}_e(\mathbf{x})|$, and its distribution is, as introduced above, denoted by $p_e(v)$. The magnitude of $\mathbf{q}(\mathbf{x})$ is denoted by $q(\mathbf{x})$. The advective tortuosity can be determined as $\chi = \langle q(\mathbf{x})\rangle/\langle q_1(\mathbf{x})\rangle$ [39], where the overbar denotes the spatial and ensemble average. Based on (4), the Eulerian velocity distribution is given in terms of the distribution $p_q(q)$ of $q(\mathbf{x})$ as

$$p_e(v) = p_q(v/v_0)/v_0. \qquad\qquad (5)$$

In this work, hydraulic conductivity is represented by a three-dimensional lognormally distributed spatial random field. The horizontal correlation length is $\ell_h \approx 5\ell_v$ and the variance of the logarithm $f(\mathbf{x}) = \ln[K(\mathbf{x})]$ of hydraulic conductivity is set to $\sigma_f^2 = 5.9$ reflecting the conductivity statistics estimated for the MADE site [49]. Figure 1 shows the empirical distributions of $f(\mathbf{x}) = \ln[K(\mathbf{x})]$ and $\nu(\mathbf{x}) = \ln[q(\mathbf{x})]$. We find for the advective tortuosity $\chi = 1.15$. The distribution $p_\nu(\nu)$ of $\nu(\mathbf{x})$ can be modeled by the skewed Gaussian distribution

$$p_\nu(\nu) = \frac{\exp\left[-\frac{(\nu-m)^2}{2\sigma_\nu^2}\right]}{\sqrt{2\pi\sigma_\nu^2}}\Phi[\alpha(\nu - m)/\sqrt{\sigma_\nu^2}], \qquad\qquad (6)$$

where $\Phi(x)$ is the cumulative unit Gaussian distribution. The parameters in Figure 1 are $\sigma_\nu^2 = \sigma_f^2 = 5.9$, $\alpha = 1.29$ and $m = 1.47$.

Regarding the propagation of the particle speeds $v_\ell(s)$, the key feature is the spatial persistence of speeds, which is characteristic for transport in steady flow fields [19, 22, 42, 48]. This spatial persistence is at the origin of intermittent Lagrangian flow properties in porous media found both at the pore and Darcy scales [38, 45, 50, 51]. Thus velocity transitions have been modeled, for example through independent sampling after fixed persistence lengths [13], Bernoulli processes [11, 38, 48], and by empirical velocity transition matrices [42, 43]. In this work, we use an Ornstein-Uhlenbeck process in order to propagate the particle velocities $v_\ell(s)$ from their initial values $v_0 = v_\ell(0)$. This process has been used and verified for the prediction of equidistant Lagrangian velocity series and intermittent transport characteristics in pore and Darcy scale heterogeneous porous media [38, 39, 45, 51].

The Ornstein-Uhlenbeck process describes the evolution of the normal score $w(s)$ of $v_\ell(s)$, which is given by

$$w = \Phi^{-1}[P_v(v)], \qquad\qquad\qquad v = P_v^{-1}[\Phi(w)]. \qquad\qquad (7)$$

The cumulative probability of $p_v(v)$ is denoted by $P_v(v)$, its inverse by $P_v^{-1}(v)$. The normal score $w(s)$ evolves according to the Ornstein-Uhlenbeck process [52]

$$\frac{dw(s)}{ds} = -\ell_c^{-1}w(s) + \sqrt{2\ell_c^{-1}}\eta(s), \qquad\qquad (8)$$

where $\eta(s)$ is a Gaussian white noise characterized by 0 mean and correlation $\langle\eta(s)\eta(s')\rangle = \delta(s - s')$. The steady state distribution of $w(s)$ is the unit Gaussian. The initial values $w(0)$ of the normal scores are obtained from $v(0)$ through the Smirnov transform (7). The initial velocity distribution is denoted by $p_0(v)$. The correlation length ℓ_c of the normal score $w(s)$ is set equal to $\ell_c = 8\ell_h/3$ [22, 38, 39].

Equations (1) together with the evolution equation for $v_\ell(s)$, describe the propagation of the particle position $x(s)$ and velocity $v_\ell(s)$ from the initial values $x(0)$, and $v(0)$, which are distributed according to $\rho(x)$, and $p_0(v)$. The
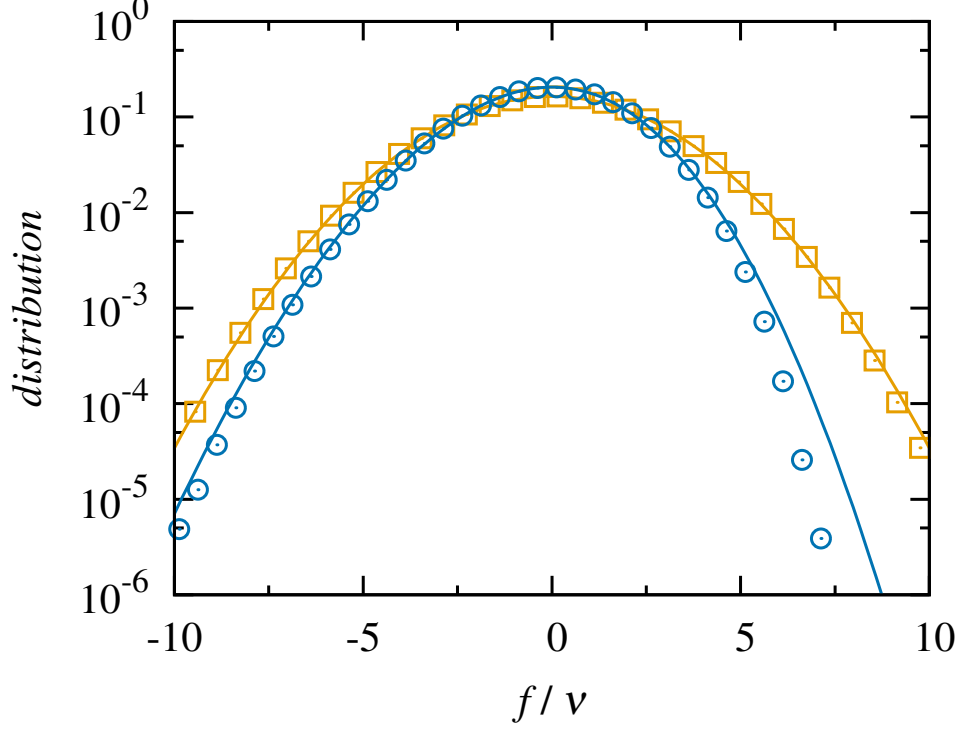
Figure 1. (Squares) empirical distribution of $f(\mathbf{x})$. The solid orange line denotes the normal distribution with zero mean and variance $\sigma_f^2 = 5.9$. (Circles) empirical distribution of the logarithm $\nu(\mathbf{x})$ of the flow speed. The blue solid line denotes the skewed normal distribution (6).

initial value of time is $t(0) = 0$. The projected streamwise concentration profile $c(x,t)$ of the mobile, this means non-adsorbed solute in this framework is obtained by

$$c(x,t) = \theta^{-1} \left\langle \delta \left[x - s(t)/\chi \right] \right\rangle, \tag{9}$$

where $s(t) = \max[s|t_a(s) \leq t]$. The angular brackets denote here the average over all particles. Note that the TDRW approach is intrinsically mass conservative. Thus its density describes the total, this means adsorbed and non-adsorbed concentrations, which is the reason why the non-adsorbed concentration is obtained from the total density through division by θ as given in (9).

B. Stochastic mobile-immobile mass transfer

The model can be extended to account for mobile-immobile mass transfer by subordination of the advective particle motion described by Eq. (1) using a compound Poisson process [53], $\tau_c(t)$, for trapping events that occur at constant rate γ and whose random duration τ_f is distributed according to $\psi_f(t)$. The particle time $t(s)$ is then given by

$$t(s) = t_a(s) + \tau_c[t_a(s)], \qquad\qquad \tau_c(t) = \sum_{i=1}^{n_t} \tau_{f,i}, \tag{10}$$

where n_t is a Poissonian random variable that denotes that number of trapping events that occur at constant rate during the time t. The advection time $t_a(s)$ is obtained by integration of Eq. (1) from 0 to s. The mobile concentration is then given by

$$g_m(x,t) = \int_0^t dt' c(x,t') \psi_c(t - t'|t'), \tag{11}$$

where $\psi_c(t|t')$ is the distribution of the compound Poisson process $\tau_c(t')$. Thus, the integrand on the right side of expression (11) denotes the probability $c(x, t')$ that a particle is at x at the advective time t' times the probability $\psi_c(t - t'|t')$ that the compound trapping time is $t - t'$. The concentration $g_{im}(x, t)$ of immobile, this means trapped particles is given in terms of the concentration $g_m(x, t)$ of mobile particles by

$$g_{im}(x, t) = \int_0^t dt' \gamma g_m(x, t') \Psi_f(t - t'), \qquad\qquad \Psi_f(t) = \int_t^\infty dt' \psi_f(t'). \qquad (12)$$

see Appendix B. The integrand on the right side denotes the probability per time that a particle gets trapped at t', $\gamma g_m(x, t')$, times the probability $\Psi_f(t - t')$ that the trapping time is larger than $t - t'$. The latter is related to the memory function $\varphi(t)$ in the multirate mass transfer formulations of Haggerty and Gorelick [17] and Harvey and Gorelick [28] as

$$\varphi(t) = \frac{1}{\langle \tau_f \rangle} \Psi_f(t). \qquad (13)$$

The capacity coefficient β of Haggerty and Gorelick [17] is given in terms of the trapping rate and the mean trapping time as $\beta = \gamma \langle \tau_f \rangle$. Similar implementations were employed by Margolin *et al.* [40], Benson and Meerschaert [41] and Comolli *et al.* [54].

In the following, we use this upscaled transport model to predict the longitudinal plume evolution of the MADE-1 experiment. The numerical implementation is detailed in Appendix A. The upscaled model described above is fully defined by the speed distribution $p_q(q)$, advective tortuosity χ, the correlation length ℓ_c, as well as porosity ϕ and retardation coefficient θ. We distinguish between these parameters, which determine the way the system is propagated, and the initial data for particle positions and velocities, which depend on the injection conditions and on the details of the heterogeneity distribution at the injection region.

III. PREDICTION OF DISPERSION AT THE MADE SITE

We use the upscaled transport model presented in the previous section for the prediction of the streamwise tracer profiles of the MADE-1 and MADE-2 experiments [7, 55]. For the MADE-1 experiment, we consider six snapshots of the longitudinal bromide concentration profiles [7, 37], for the MADE-2 experiment, we consider two snapshots of the longitudinal tritium profiles [32, 55]. In the following, we first discuss the model parameters for the MADE site, and then report on the prediction of the longitudinal concentration profiles for the MADE-1 and MADE-2 experiments.

A. Hydraulic and transport parameters for the MADE site

We consider purely advective transport, which is a reasonable assumption given that the Péclet number at the MADE site is around 10^3 [37]. In order to parameterize the model, we rely on the description of the experimental conditions in Boggs *et al.* [12] and Adams and Gelhar [7] and the geostatistical characterization of the hydraulic conductivity field given in Bohling *et al.* [49]. Thus, the medium porosity, and the magnitude of the mean hydraulic gradient are set equal to $\phi = 0.31$, $J = 3.6 \times 10^{-3}$ [7, 12, 37]. Bohling *et al.* [49] estimate for the variance of the logarithm of conductivity $\sigma_f^2 = 5.9$ and for the horizontal and vertical correlation length $\ell_h = 9.1$ m and $\ell_v = 1.8$ m. For the geometric mean conductivity these authors obtain the value $K_g = 6.7 \times 10^{-6}$ m/s. Here we use the value $K_g = 5.5 \times 10^{-6}$ m/s, which is between the lower limit of the 95 % confidence interval $K_g = 4.3 \times 10^{-6}$ m/s and $K_g = 6.7 \times 10^{-6}$ m/s. These values are summarized in Table I. The characteristic velocity v_0 is thus given by $v_0 = 5.32 \times 10^{-8}$ m/s. We use for the prediction of both the MADE-1 and MADE-2 data the same medium and hydraulic parameters. However, the retardation coefficient for bromide (MADE-1) is set is equal to $\theta = 1.2$, while the retardation coefficient for tritium (MADE-2) is set to $\theta = 1$ [56]. The retardation coefficient accounts for the fact that the only the mobile, non-adsorbed solute is measured [28, 56], and in this sense accounts for a measurement bias.

The parameter values specified above determine the propagator of the upscaled transport model. In order to predict the plume evolution, we need both the propagator, and the initial conditions, this means here, the initial particle positions, i.e., initial tracer distribution, and initial particle speed distribution. As described in Boggs *et al.* [12] and Stauffer *et al.* [57], in both experiments tracer was injected into five 5.2-cm-diameter injection wells separated by 1 m in a linear array perpendicular to the mean flow direction. This justifies the use of a pointlike initial particle distribution, localized at the origin at $x = 0$,

$$\rho(x) = \delta(x). \qquad (14)$$

Parameter	σ_f^2	K_g [m/s]	ℓ_h [m]	ℓ_v [m]	J [-]	ϕ	θ [Br]	θ [^{3}H]
Value	5.9	5.5×10^{-6}	9.1	1.8	3.6×10^{-3}	0.31	1.2	1

Table I. Geostatistical, and hydraulic data for the MADE site, as well as retardation coefficients for the bromide and tritium tracers of the MADE-1 and MADE-2 experiment according to Bohling *et al.* [49], Boggs *et al.* [12] and Boggs and Adams [56].
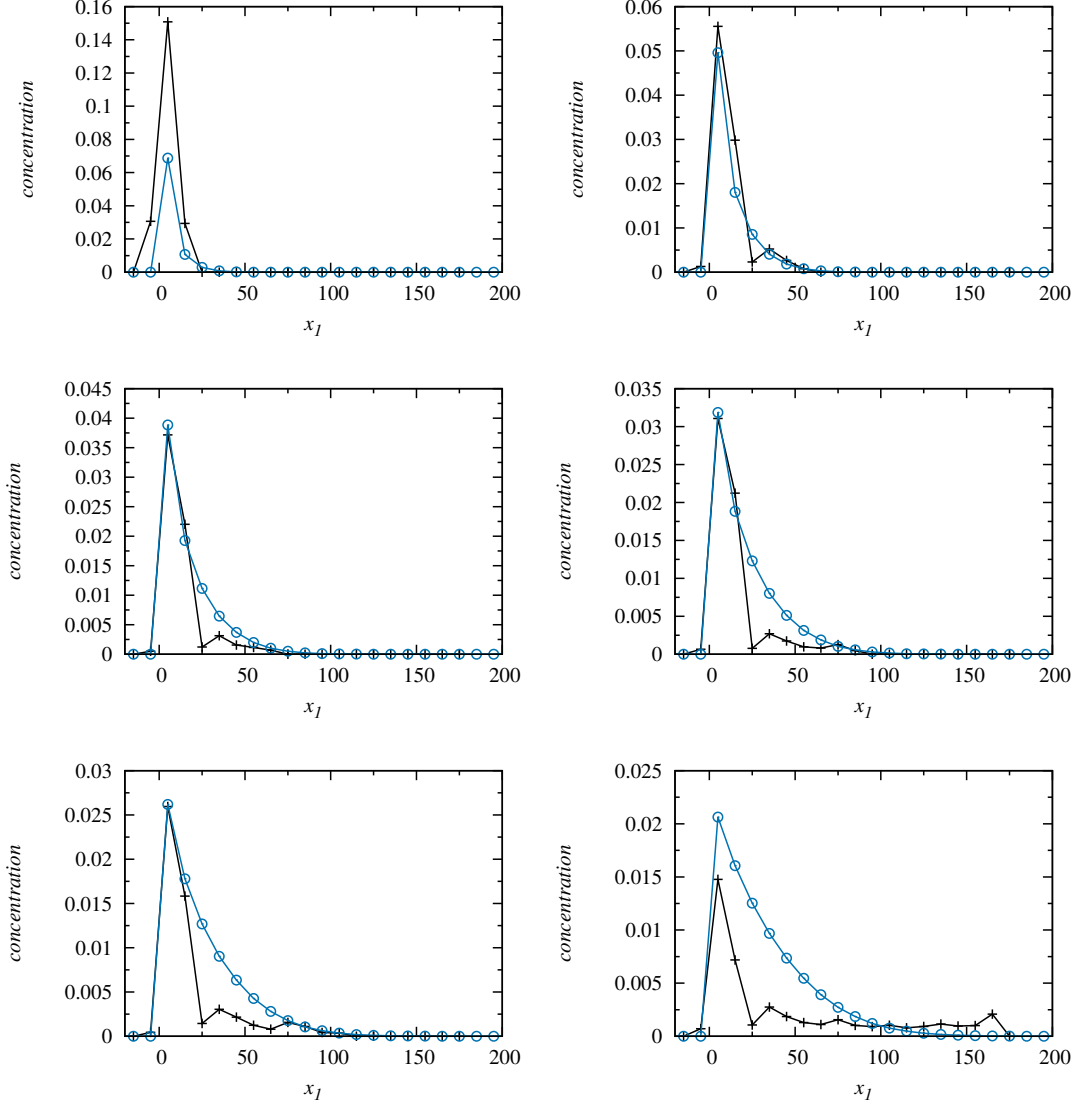

Figure 2. Concentration profiles from the (black crosses) MADE-1 data and the upscaled model for an averaging window of (blue circles) $\Delta x = 10$ m at times (top left to bottom right) $t = 49$ d, 126 d, 202 d, 279 d, 370 d and 503 d using a pointlike initial distribution.

In both experiments, tracer was injected in about 10 m^3 of groundwater for the duration of 48.5 hours. However, we employ for the sake of simplicity the pointlike initial condition (14). Regarding the initial velocity distribution $p_0(v)$, we note that Boggs *et al.* [12] and Fiori *et al.* [37] pointed out that more mass entered in the high than in the low conductivity zones, which implies that the initial mass distribution is approximately flux-weighted. The flux-weighted Eulerian speed distribution is equal to $p_v(v)$, see Eq. (2). Thus, we set $p_0(v) = p_v(v)$.

Below we use this approach to model and predict the longitudinal concentration profiles of the MADE-1 and MADE-2 experiments. We also assess the possible impact of mobile-immobile mass transfer as suggested by Harvey and Gorelick [28]. To this end, we use the mass transfer parameters estimated by these authors by fitting a mass transfer model to the experimental data for the evolution of the total mass. Specifically, we use the exponential memory
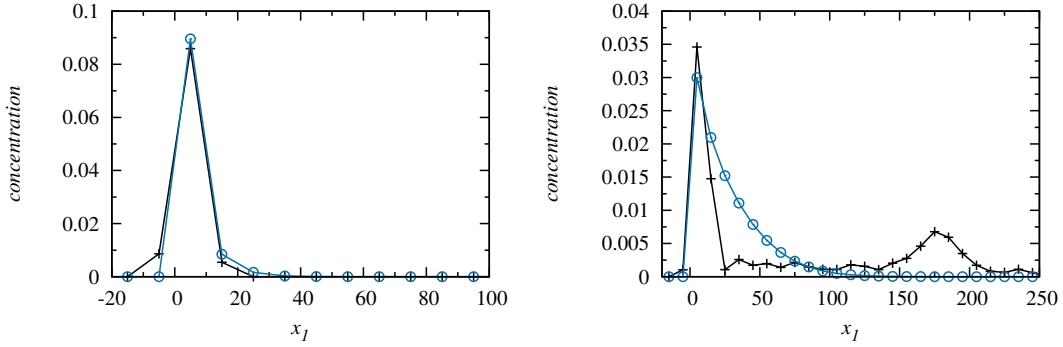
Figure 3. Concentration profiles from the (black crosses) MADE-2 data and the upscaled model for an averaging window of (blue circles) $\Delta x = 10$ m at times (left panel) $t = 27$ d and (right panel) 328 d using a pointlike initial distribution.

function $\varphi(t) = \alpha \exp(-\alpha t)$ with $\alpha = 4.6 \times 10^{-3}$ d^{-1} for bromide, $\alpha = 1.1 \times 10^{-2}$ d^{-1} for tritium, and the capacity coefficient $\beta = 6$. In our stochastic modeling framework, these parameters correspond to the exponential trapping time distribution $\psi_f(t) = \alpha \exp(-\alpha t)$ and the trapping rate $\gamma = \beta\alpha$. Note that Harvey and Gorelick [28] develop an analytical expression for the total mass that accounts for mobile-immobile mass transfer, and a measurement bias due to mass detection in the mobile zones only. The capacity coefficient β and rate α are obtained by fitting this expression to the mass data of the MADE-1 and MADE-2 experiments.

B. Longitudinal concentration profiles

The experimental concentration profiles for the MADE-1 experiment are based on the bromide tracer data from Adams and Gelhar [7] normalized to the initial mass as given in Fiori *et al.* [37]. The concentration profiles for the tritium tracer at the MADE-2 experiment are obtained from Salamon *et al.* [32].

Figure 2 and 3 show the experimental and predicted longitudinal concentration distributions. As explained in Adams and Gelhar [7] and Salamon *et al.* [32], the displayed data was obtained by interpolation of concentration values between sampling wells, vertical and transverse integration of the resulting concentration field, and longitudinal averaging over a window of $\Delta x = 10$ m [7, 32]. The bin centers are located at $x_i = -15$ m $+ i10$ m with $i = 0, \ldots, 19$. The injection positions is at $x = 0$. Concentration values are normalized by the initial mass. The longitudinal concentration distribution is shown at six snapshots at times $t = 49, 126, 202, 279, 370$ and 503 days for MADE-1 and at $t = 27$ and 328 d for MADE-2. The tracer distributions predicted from the upscaled model are presented in the same way. Appendix D provides the tracer distributions with an averaging window of $\Delta x = 10^{-1}$ m for MADE-1. We refer to the latter as the fine scale model data.

We first note that the experimental data does not integrate to 1. In fact the mass under the longitudinal profiles for the MADE-1 data integrates to $2.06, 0.99, 0.68, 0.62, 0.54$ and 0.43 for the six snapshots at increasing time [7, 37] and to 1.52 and 0.77 at $t = 27$ d and 328 d for the MADE-2 snapshots [57]. The explanation of this apparent mass loss has been a matter of debate in the literature. Several authors [28, 32, 56, 58] attribute the overestimation of mass at early, and understimation at late times to a measurement bias due to preferential sampling of high concentrations from high conductivity regions, which can also explain strong downstream tailing observed for the 503 d snapshot of the MADE-1 and the 328 d snapshot of the MADE-2 data. Other authors [7, 37] debate that the mass loss could be attributed to a decreasing density of sampling points at distances larger than 20 m downstream from the injection region. This view is supported by the fact that more mass loss is observed for the bromide plume in the MADE-1 [7] than for the tritium plume in the MADE-2 experiment [57], for which the density of sampling wells was increased. In this study, we do not enter in this debate, but investigate whether large scale features of the observed tracer plumes such as the slow moving peak, and significant forward tailing, can be predicted by an upscaled model based on hydraulic aquifer parameters.

The tracer distribution in the upscaled model is by default normalized to 1 and predicts the overall shape of the observed tracer distributions. The slow moving peak and its value are in general well captured for both the MADE-1 and MADE-2 data as discussed below and in Appendix E. The upscaled model also predicts the development of the forward tail with increasing time. While the predicted mass in the tails for the MADE-1 data is generally higher than for the experimental data, the reach is relatively well reproduced for all except for the snapshot at 503 d, see also the corresponding logarithmic plots in Appendix D. The last snapshots at $t = 503$ d for the MADE-1 and $t = 328$
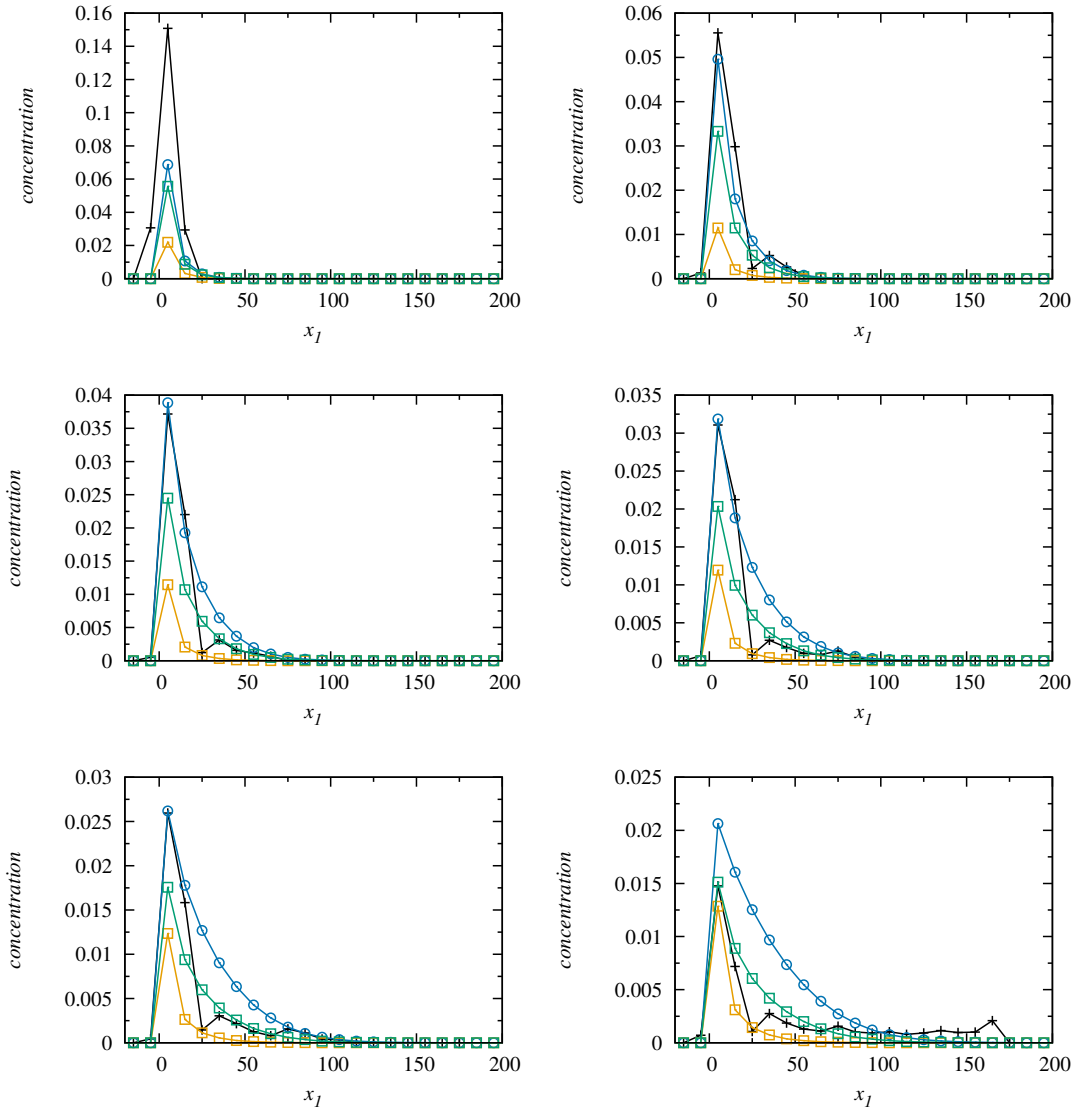
Figure 4. Concentration profiles from the (black crosses) MADE-1 data and model predictions for (blue circles) the advective TDRW model, and the TDRW with mobile-immobile mass transfer using (orange squares) $\beta = 6$ and (green) squares $\beta = 1$. The observation times and averaging window are the same as in the previous figure.

d for the MADE-2 experiments show farther reaching forward tails, which are not captured by the TDRW model. However, as mentioned above, the observed strong downstream tailing may be attributed to sampling bias.

The TDRW approach quantifies retention of tracer mass in the injection region through persistent low initial flow speeds. The forward tailing is caused by the presence of high initial flow velocities, in combination with fast tracer motion through particle transitions into spatially persistent fast velocity channels. The higher the proportion of low flow speeds in the initial distribution, the higher the peak. On the other hand, the higher the proportion of high velocities in the initial speed distribution $p_0(v)$ and in the propagator $p_v(v)$, the more pronounced is the forward tail. This is illustrated in the concentration profiles for different values of K_g in the supplemental material.

In order to assess the impact of mass transfer on these concentration profiles, we show in Figures 4 and 5 the predictions of the TDRW model combined with mobile-immobile mass transfer for the MADE-1 and MADE-2 data. The models using a capacity coefficient of $\beta = 6$ underestimate the observed peak concentrations at all snapshots. Thus, we adjust the capacity coefficient to $\beta = 1$ to fit the concentration snapshot at $t = 503$ d for the MADE-1 experiment in the spirit of Harvey and Gorelick [28], who model this concentration data using a multirate mass transfer model. While $\beta = 1$ provides a good fit for 503 d, it underestimates the peak concentrations values at all other observation times. For the MADE-2 data, we observe a similar behavior. Note that Harvey and Gorelick [28]
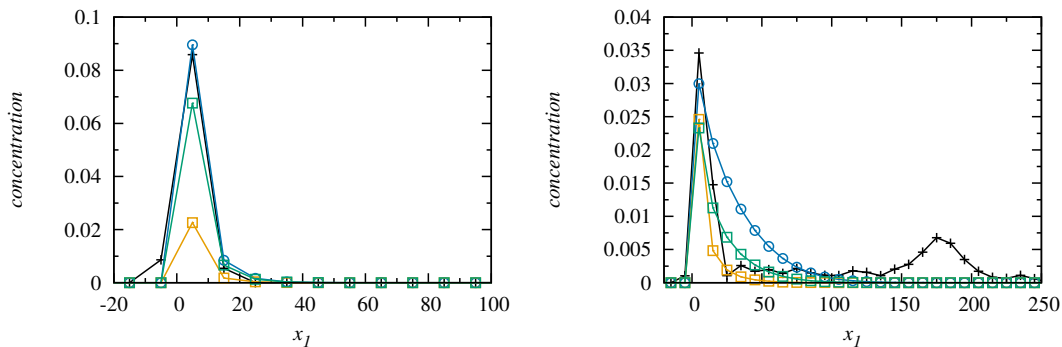
Figure 5. Concentration profiles from the (black crosses) MADE-2 data and model predictions for (blue circles) the advective TDRW model, and the TDRW with mobile-immobile mass transfer using (orange squares) $\beta = 6$ and (green) squares $\beta = 1$. The observation times and averaging window are the same as in Figure 3.

adjusted the mobile-immobile parameter to the total mass evolution, and the parameters of an analytical accelerating flow model from the observed concentration profiles. In our approach, advective transport is fully determined by the medium and Eulerian flow properties. Thus, while the mobile-immobile mass transfer approach can fit the apparent mass decay [28], it is, at least within the proposed framework, not able to describe the evolution of the shape of the tracer plume. As we have seen, the purely advective upscaled model predicts the salient large scale features of non-Fickian solute transport based on spatial variablity of hydraulic conductivity and flow heterogeneity.

IV.   CONCLUSIONS

We have presented a Lagrangian stochastic model for transport in heterogeneous aquifers that is parameterized in terms of the statistical characteristics of hydraulic conductivity and Eulerian flow speed. The approach is based on a Markov processes for equidistant particle velocities, whose steady state distribution is given by the flux-weighted flow speed distribution. The latter is derived from the distribution of the Eulerian flow speed, which is obtained from standardized numerical flow simulations, this means, for unit gradient of hydraulic head and unit geometric mean conductivity. The model is parameterized by the mean, variance and correlation lengths of the logarithm of hydraulic conductivity, advective tortuosity, porosity, and a retardation coefficient. These model inputs are transport independent, this means they can be assessed by medium and flow characterization. Furthermore, mobile-immobile mass transfer is accounted for by a compound Poisson process. We show the equivalence of this formulation with Eulerian multirate mass transfer formulations. These features yield a predictive upscaled approach for advective tracer transport in heterogeneous aquifers combined with mobile-immobile mass transfer. Like other stochastic models, this approach relies on the ergodicity of the underlying medium heteorgeneity. Furthermore, the model is currently limited to purely advective mobile transport.

We use this upscaled model to assess and predict the evolution of the bromide tracer plume of the MADE-1 and the tritium plume of the MADE-2 experiments, which are characterized by strongly non-Gaussian shapes. Relatively low conductivity in the source zone leads to slow peak movement of only a few meters over the duration of the experiments, while part of the tracer moves fast, which gives rise to a pronounced forward tail. The slow moving peak is captured by the upscaled model through the low velocity end in the distribution of initial particle speeds. The developing forward tail is quantified by tracer propagation due to spatially persistent broadly distributed particle speeds. The speed distributions are determined by the medium and Eulerian flow statistics. As mentioned above all model parameters are obtained from transport independent measurements, without recourse to fitting parameters. We find that the purely advective upscaled model provides a robust estimate of the evolution of the overall plume shape. This indicates that the large scale transport features may be explained by flow heterogeneity due to spatial variability in hydraulic conductivity. The proposed upscaled model is predictive, transferable to different solutes and hydraulic conditions, and seems to capture the salient heterogeneity mechanisms, and their impact on large scale transport.

ACKNOWLEDGMENTS

[1] J. Bear, *Dynamics of Fuids in Porous Media* (American Elsevier, New York, 1972).
[2] L. W. Gelhar and C. L. Axness, Water Resour. Res. **19**, 161 (1983).
[3] G. Dagan, J. Fluid Mech. **145**, 151 (1984).
[4] G. Dagan, *Flow and transport in porous formations* (Springer, New York, 1989).
[5] L. W. Gelhar, *Stochastic subsurface hydrology* (Prentice Hall, 1993).
[6] Y. Rubin, *Applied stochastic hydrogeology* (Oxford University Press, New York, 2003).
[7] E. E. Adams and L. W. Gelhar, Water Resour. Res. **28**, 3293 (1992).
[8] M. Levy and B. Berkowitz, Journal of Contaminant Hydrology **64**, 203 (2003).
[9] R. Haggerty, S. A. McKenna, and L. C. Meigs, Water Resour. Res. **36**, 3467 (2000).
[10] C. Zheng, M. Bianchi, and S. M. Gorelick, Groundwater **49**, 649 (2011).
[11] P. K. Kang, T. Le Borgne, M. Dentz, O. Bour, and R. Juanes, Water Resour. Res. **51**, 940 (2015).
[12] J. M. Boggs, S. C. Young, L. M. Beard, L. W. Gelhar, K. R. Rehfeldt, and E. E. Adams, Water Resour. Res. **28**, 3281 (1992).
[13] B. Berkowitz, A. Cortis, M. Dentz, and H. Scher, Rev. Geophys. **44**, RG2003 (2006).
[14] S. P. Neuman and D. M. Tartakovsky, Adv. Water Resour. **32**, 670 (2008).
[15] M. Dentz, T. Le Borgne, A. Englert, and B. Bijeljic, J. Cont. Hydrol. **120-121**, 1 (2011).
[16] B. Noetinger, D. Roubinet, A. Russian, T. Le Borgne, F. Delay, M. Dentz, J.-R. De Dreuzy, and P. Gouze, Transport in Porous Media , 1 (2016).
[17] R. Haggerty and S. M. Gorelick, Water Resour. Res. **31**, 2383 (1995).
[18] J. Carrera, X. Sánchez-Vila, I. Benet, A. Medina, G. Galarza, and J. Guimerà, Hydrogeology Journal **6**, 178 (1998).
[19] B. Berkowitz and H. Scher, Phys. Rev. Lett. **79**, 4038 (1997).
[20] D. A. Benson, S. W. Wheatcraft, and M. M. Meerschaert, Water Resources Research **36**, 1403 (2000).
[21] J. H. Cushman and T. R. Ginn, Water Resour. Res. **36**, 3763 (2000).
[22] V. Cvetkovic, H. Cheng, and X.-H. Wen, Water Resour. Res. **32**, 1671 (1996).
[23] A. Fiori, I. Jankovic, G. Dagan, and V. Cvetkovic, Water Resour. Res. **43**, W09407 (2007).
[24] J. Cushman and T. Ginn, Transp. Porous Media **13**, 123 (1993).
[25] S. P. Neuman, Water Resour. Res **29**, 633 (1993).
[26] B. Berkowitz and H. Scher, Phys. Rev. E **57**, 5858 (1998).
[27] R. Schumer, D. A. Benson, M. M. Meerschaert, and B. Bauemer, Water Resour Res **39(10)**, 1296 (2003).
[28] C. Harvey and S. M. Gorelick, Water Resources Research **36**, 637 (2000).
[29] C. E. Feehley, C. Zheng, and F. J. Molz, Water Resources Research **36**, 2501 (2000).
[30] J. Guan, F. J. Molz, Q. Zhou, H. H. Liu, and C. Zheng, Water Resources Research **44** (2008), 10.1029/2007wr006120.
[31] H. C. Barlebo, M. C. Hill, and D. Rosbjerg, Water Resour. Res. **40**, W04211 (2004).
[32] P. Salamon, D. Fernàndez-Garcia, and J. J. Gómez-Hernández, Water Resour. Res. **43**, W08404 (2007).
[33] M. Dogan, R. L. Van Dam, G. Liu, M. M. Meerschaert, J. J. Butler Jr., G. C. Bohling, D. A. Benson, and D. W. Hyndman, Geophys. Res. Lett. **41**, 7560 (2016).
[34] V. Cvetkovic, A. Fiori, and G. Dagan, Water Resources Research **50**, 5759 (2014).
[35] Y. Edery, A. Guadagnini, H. Scher, and B. Berkowitz, Water Resour Res **50 (2)**, 1490 (2014).
[36] A. Tyukhova, M. Dentz, W. Kinzelbach, and M. Willmann, Physical Review Fluids **1**, 074002 (2016).
[37] A. Fiori, G. Dagan, I. Jankovic, and A. Zarlenga, Water Resources Research **49**, 2497 (2013).
[38] V. Hakoun, A. Comolli, and M. Dentz, Water Resour. Res. **55**, 10.1029/2018WR023810 (2019).
[39] A. Comolli, V. Hakoun, and M. Dentz, Water Resources Research **55**, 8197 (2019).
[40] G. Margolin, M. Dentz, and B. Berkowitz, Chem. Phys. **295**, 71 (2003).
[41] D. A. Benson and M. M. Meerschaert, Adv. Wat. Res. **32 (4)**, 532 (2009).
[42] T. Le Borgne, M. Dentz, and J. Carrera, Phys. Rev. E **78**, 041110 (2008).
[43] P. K. Kang, M. Dentz, T. Le Borgne, and R. Juanes, Phys. Rev. Lett. **107**, 180602 (2011).
[44] P. K. Kang, P. de Anna, J. Nunes, B. Bijeljic, M. J. Blunt, and R. Juanes, Geophys. Res. Lett. **41 (17)**, 6184 (2014).
[45] V. L. Morales, M. Dentz, M. Willmann, and M. Holzner, Geophysical Research Letters **44**, 9361 (2017).

[46] P. K. Kang, M. Dentz, T. Le Borgne, S. Lee, and R. Juanes, Adv. Water Resour. (2017), 10.1016/j.advwatres.2017.03.024.
[47] J. D. Hyman, M. Dentz, A. Hagberg, and P. K. Kang, Journal of Geophysical Research: Solid Earth (2019), 10.1029/2018jb016553.
[48] M. Dentz, P. K. Kang, A. Comolli, T. Le Borgne, and D. R. Lester, Physical Review Fluids **1**, 074004 (2016).
[49] G. C. Bohling, G. Liu, P. Dietrich, and J. J. Butler, Water Resources Research **52**, 8970 (2016).
[50] P. de Anna, T. Le Borgne, M. Dentz, A. M. Tartakovsky, D. Bolster, and P. Davy, Phys. Rev. Lett. **110**, 184502 (2013).
[51] A. Puyguiraud, P. Gouze, and M. Dentz, Water Resources Research **55**, 1196 (2019).
[52] C. W. Gardiner, Applied Optics **25**, 3145 (1986).
[53] W. Feller, *An Introduction to Probability Theory and Its Applications*, Wiley Series in Probability and Statistics, Vol. 1 (Wiley, 1968).
[54] A. Comolli, J. J. Hidalgo, C. Moussey, and M. Dentz, Transport in Porous Media **115**, 265 (2016).
[55] J. Boggs, L. Beard, W. Waldrop, T. Stauffer, W. MacIntyre, and C. Antworth, *Transport of tritium and four organic compounds during a natural-gradient experiment (MADE-2)*, Tech. Rep. (Electric Power Research Inst., Palo Alto, CA (United States); Tennessee Valley Authority, Norris, TN (United States). Engineering Lab.; Air Force Engineering and Services Center, Tyndall AFB, FL (United States), 1993).
[56] J. M. Boggs and E. E. Adams, Water Resources Research **28**, 3325 (1992).
[57] T. B. Stauffer, C. P. Antworth, R. G. Young, W. G. MacIntyre, and J. Boggs, *Degradation of aromatic hydrocarbons in an aquifer during a field experiment demonstrating the feasibility of remediation by natural attenuation*, Tech. Rep. (TENNESSEE VALLEY AUTHORITY NORRIS, 1994).
[58] F. J. Molz, C. Zheng, S. M. Gorelick, and C. F. Harvey, Water Resources Research **42** (2006), 10.1029/2005wr004265.
[59] F. Ruan and D. McLaughlin, Advances in Water Resources **21**, 385 (1998).
[60] M. Abramowitz and I. A. Stegun, *Handbook of Mathematical Functions* (Dover Publications, New York, 1972).

Appendix A: Flow solution

The hydraulic conductivity fields are generated using the spectral method of Ruan and McLaughlin [59] with an exponential covariance function. The flow problem (3) is solved numerically using a two-point flux finite volume method in 40 realizations of $f(\mathbf{x})$ whose spatial mean and variance are within a 0.05 tolerance interval around the target values of 0 and 5.9. The flow domains have the dimensions $20\lambda_h$ in the direction of the mean gradient, $10\lambda_h$ in the transverse horizontal direction, and $10\lambda_v$ in vertical direction. The resolution is $2^8 \times 2^7 \times 2^5$ voxels.

Appendix B: Stochastic mobile-immobile mass exchange

The solute concentration in the advective time-domain random walk framework is given by (9). It can be expanded into

$$c(x,t) = \theta^{-1} \int\limits_0^\infty ds\, \delta[x - s/\chi] h(s,t), \tag{B1}$$

where we defined

$$h(s,t) = \langle \delta[s - s(t)] \rangle. \tag{B2}$$

It denotes the distribution of streamline distance s over which a particle has been advected at time t. The latter is related to the distribution $f(t,s) = \langle \delta[t - t_a(s)] \rangle$ of advective travel times via

$$\int\limits_s^\infty ds'\, h(s',t) = \int\limits_0^t dt\, f(t',s). \tag{B3}$$

The advective travel time is given by integration of expression (1) as

$$t_a(s) = \int\limits_0^s \frac{ds'}{v_\ell(s')}. \tag{B4}$$

Using (B3), we can write

$$c(x,t) = -\theta^{-1} \int\limits_0^\infty ds\, \delta(x - s/\chi) \frac{\partial}{\partial s} \int\limits_0^t dt'\, f(t',s) \tag{B5}$$

The latter reads in Laplace space as

$$c^*(x,s) = -\theta^{-1}\frac{1}{\lambda}\int_0^\infty ds\,\delta(x - s/\chi)\frac{\partial}{\partial s}f^*(\lambda,s). \tag{B6}$$

The Laplace transform is defined in Abramowitz and Stegun [60], the Laplace variable is λ. The Laplace transform of $f(t,s)$ can be written as

$$f^*(\lambda,s) = \langle\exp[-\lambda t_a(s)]\rangle. \tag{B7}$$

In the presence of trapping events that occur at constant rate, we distinguish between the clock time $t(s)$ at a given distance s, and the advection time $t_a(s)$. The clock time, given by (10), is the sum of $t_a(s)$ and the compound trapping time $\tau_c[t_a(s)]$. In analogy to (B6), the total solute concentration $g(x,t)$ under mobile-immobile mass transfer is given by

$$g(x,t) = -\theta^{-1}\int_0^\infty ds\,\delta(x - s/\chi)\frac{\partial}{\partial s}\int_0^t dt'\, f_m(t',s) \tag{B8}$$

where $f_m(t,s) = \delta[t - t(s)]$. The clock time distribution can be written as

$$f_m(t,s) = \langle\delta\left(t - t_a(s) - \tau_c[t_a(s)]\right)\rangle = \int_0^\infty dt'\langle\delta[t' - t_a(s)]\rangle\langle\delta[t - t' - \tau_c(t')]\rangle = \int_0^t dt'\, f(t',s)\psi_c(t - t'|t'), \tag{B9}$$

where $\psi_c(t|t') = \langle\delta[t - \tau_c(t')]\rangle$ is the distribution of the compound trapping time $\tau_c(t')$. Its Laplace transform is

$$\psi_c^*(\lambda|t) = \langle\exp[-\lambda(t + \sum_{i=1}^{n_t}\tau_i)]\rangle = \sum_{n=0}^\infty\frac{(\gamma t)^n}{n!}\exp(-\gamma t)\exp(-\lambda t)\psi_f^{*n} = \exp(-\gamma[1 - \psi_f^*(\lambda)]t - \lambda t). \tag{B10}$$

Thus, we obtain for the Laplace transform of $f_m(t,s)$ the expression

$$f_m^*(\lambda,s) = \int_0^\infty dt\, f(t,s)\exp(-\gamma[1 - \psi_f^*(\lambda)]t - \lambda t) = f^*(\lambda + \gamma[1 - \psi^*(\lambda)],s). \tag{B11}$$

With this result, we can write the Laplace transform of the concentration (B8) as

$$g^*(x,\lambda) = \theta^{-1}\frac{\lambda + \gamma[1 - \psi_f^*(\lambda)]}{\lambda}\left\{-\frac{1}{\lambda + \gamma[1 - \psi_f^*(\lambda)]}\int_0^\infty ds\,\delta(x - s/\chi)\frac{\partial}{\partial s}f^*(\lambda + \gamma[1 - \psi^*(\lambda)],s)\right\}. \tag{B12}$$

By comparison with (B6), we identify the expression in the curly brackets with

$$c^*(x,\lambda + \gamma[1 - \psi^*(\lambda)]) \equiv g_m^*(x,s), \tag{B13}$$

which is identical to the Laplace transform of the mobile concentration (11). Thus, the total concentration $g(x,t)$ is given by

$$g^*(x,\lambda) = \frac{\lambda + \gamma[1 - \psi_f^*(\lambda)]}{\lambda}g_m^*(x,\lambda) \equiv g_m^*(x,s) + g_{im}^*(x,s), \tag{B14}$$

where the immobile concentration is

$$g_{im}(x,t) = \gamma\frac{1 - \psi_f^*(\lambda)}{\lambda}g_m(x,\lambda). \tag{B15}$$

Its inverse Laplace transform is given by (12).

Appendix C: Numerical model implementation

In the following, we outline the basic steps of the numerical implementation of the stochastic time domain random walk model combined with mass transfer between mobile and immobile regions. First, we note that the steady state Eulerian velocity distribution $p_e(v)$ is given by the distribution show in Figure 1. The distribution $p_v(v)$ of particle speeds is obtained according to (2) by flux-weighting.

Step 1: Initialization   Initial particle velocities $v(0)$ are sampled from $p_v(v)$, particle positions $x(0)$ are chosen from the initial particle distribution $\rho(x)$, which here is $\rho(x) = \delta(x)$.

Step 2: Propagation of normal scores   The initial velocities $v(0)$ are then converted to the initial values $w(0)$ of the normal scores using the map (7). The normal scores $w(s)$ are propagated from their initial values $w(0)$ according to the Ornstein-Uhlenbeck process (8), which is discretized by using an Euler scheme. This gives

$$w(s + \Delta s) = w(s) \left(1 - \ell_c^{-1}\Delta s\right) + \sqrt{2\ell_c^{-1}\Delta s}\zeta(s), \tag{C1}$$

where $\zeta(s)$ denotes a Gaussian random variable with zero mean and unit variance. The discretization Δs is chosen much smaller than ℓ_c. Here we set $\Delta s = 10^{-1}$ m.

Step 3: Propagation of particle position and time   The particle positions are incremented at each random walk step by $\Delta s/\chi$, the particle times by $\Delta s/v_\ell(s)$,

$$x(s + \Delta s) = x(s) + \frac{\Delta s}{\chi}, \qquad\qquad t_a(s + \Delta s) = t_a(s) + \frac{\Delta s}{v_\ell(s)}. \tag{C2}$$

The current particle speed $v_\ell(s)$ is obtained according to Eq. (7).

Step 3*: Mobile-immobile mass transfer   Mobile immobile mass transfer is implemented as follows. Consider the auxiliary process

$$a_{n+1} = a_n + \tau_n, \tag{C3}$$

where $a_0 = 0$. The random time increments τ are distributed according to

$$\psi_0(t) = \gamma \exp(-\gamma t). \tag{C4}$$

The first trapping event occurs when $a_1 \leq t_a(s) < a_2$, the nth trapping event occurs when $a_n \leq t_a(s) < a_{n+1}$. At each trapping event, the clock time is incremented by the random trapping time τ_f such that

$$t(s) = t_a(s) + \sum_{n=0}^{n_{t_a(s)}} \tau_{f,i}, \tag{C5}$$

where n_t is a Poisson variable with mean γt. A particle is mobile at the observation time t if $t(s) - t \leq \Delta s/v_\ell(s)$ because the maximum difference during an advective, this means mobile step is $\Delta s/v_\ell(s)$.

Steps 2 and 3 are repeated until the maximum simulation time is reached. Particle positions are recorded at steps s if $t(s) \leq t_i$ and $t(s + \Delta s) > t_i$ with t_i the desired observation times.

Appendix D: Longitudinal concentration profiles,

Figure 6 shows the longitudinal concentration profiles from the MADE-1 data, and the model prediction in coarse and fine resolution. The comparison shows that the averaging window of $\Delta x = 10$ m introduces an artificial broadening of the peak due to oversmoothing, while the tail concentrations are nearly identical. With increasing time, as the peak width increases due to hydrodynamic dispersion, the differences between the coarse and fine scale models decrease.

Figure 7 shows the same data as in Figure 7 plotted logarithmically. The tail contains in general more mass than the experimental data, but reproduces relatively well the overall tendency except for the 503 d snapshot at which mass is recovered at larger downstream distances than predicted by the model.

Appendix E: Predictions for different values of K_g and Peak concentrations

Figure 8 compares the model predictions for $K_g = 4.3 \times 10^{-6}$ m/s, $K_g = 6.7 \times 10^{-6}$ m/s and $K_g = 5.5 \times 10^{-6}$ m/s. The peak height and peak retention increases, the forward tail decreases with decreasing K_g.
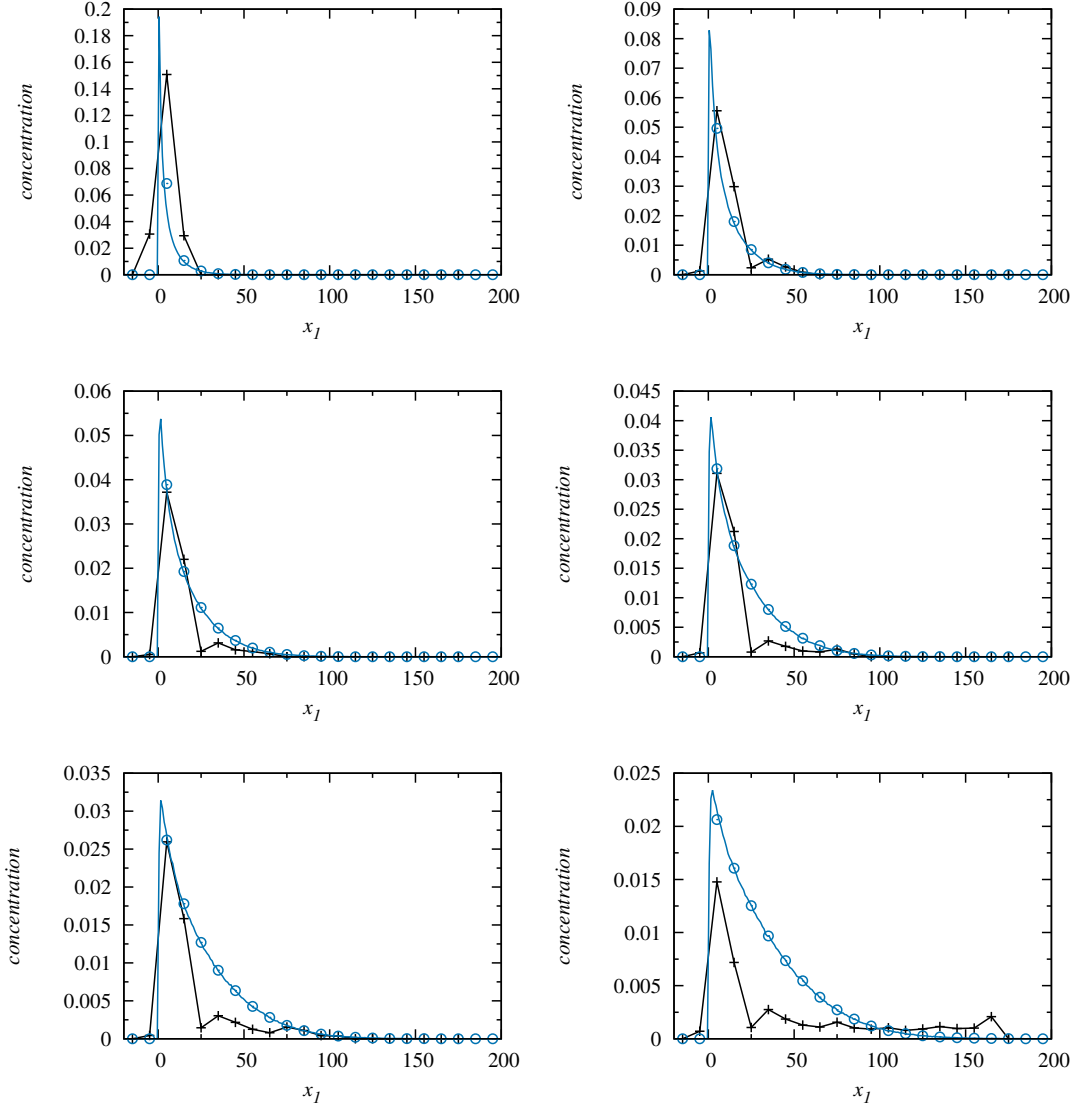
Figure 6. Concentration profiles from the (black crosses) MADE data and the upscaled model for an averaging window of (blue triangles) $\Delta x = 10$ m and (solid blue line) $\Delta x = 10^{-1}$ m at times (top left to bottom right) $t = 49$ d, 126 d, 202 d, 279 d, 370 d and 503 d using a pointlike initial distribution.

The concentration peak is localized at all snapshots at $x = 5$ m, which indicates that it does not move beyond the averaging window between $x = 0$ m and 10 m. This is supported by the fine scale prediction. The upscaled model predicts peak heights and widths that are qualitatively and quantitatively similar to the experimental observations. The peak concentrations from the experimental data, and the corresponding model predictions are displayed in Figure 9. The upscaled model predicts the overall decay of the peak concentration. The decay behavior in the localized peak is in fact a measure for the residence time in the injection region. The mass $m_0(t)$ remaining in the region between 0 m and 10 m is equal to the probability that the residence time τ_0 of a particle is larger than t,

$$m_0(t) = \int\limits_t^\infty dt'\, \psi_0(t'), \tag{E1}$$

where $\psi_0(t)$ denotes the residence time distribution. As long as the mass in the injection region of size Δx is larger than the mass in all other bins, the peak concentration is equal to $c_0(t) = m_0(t)/\Delta x$. Figure 9 shows the evolution of $c_0(t)$ from experimental data and model predictions obtained from the upscaled model. In order to highlight the impact of the value of geometric conductivity, we also plot the decay of the maximum concentration for the values
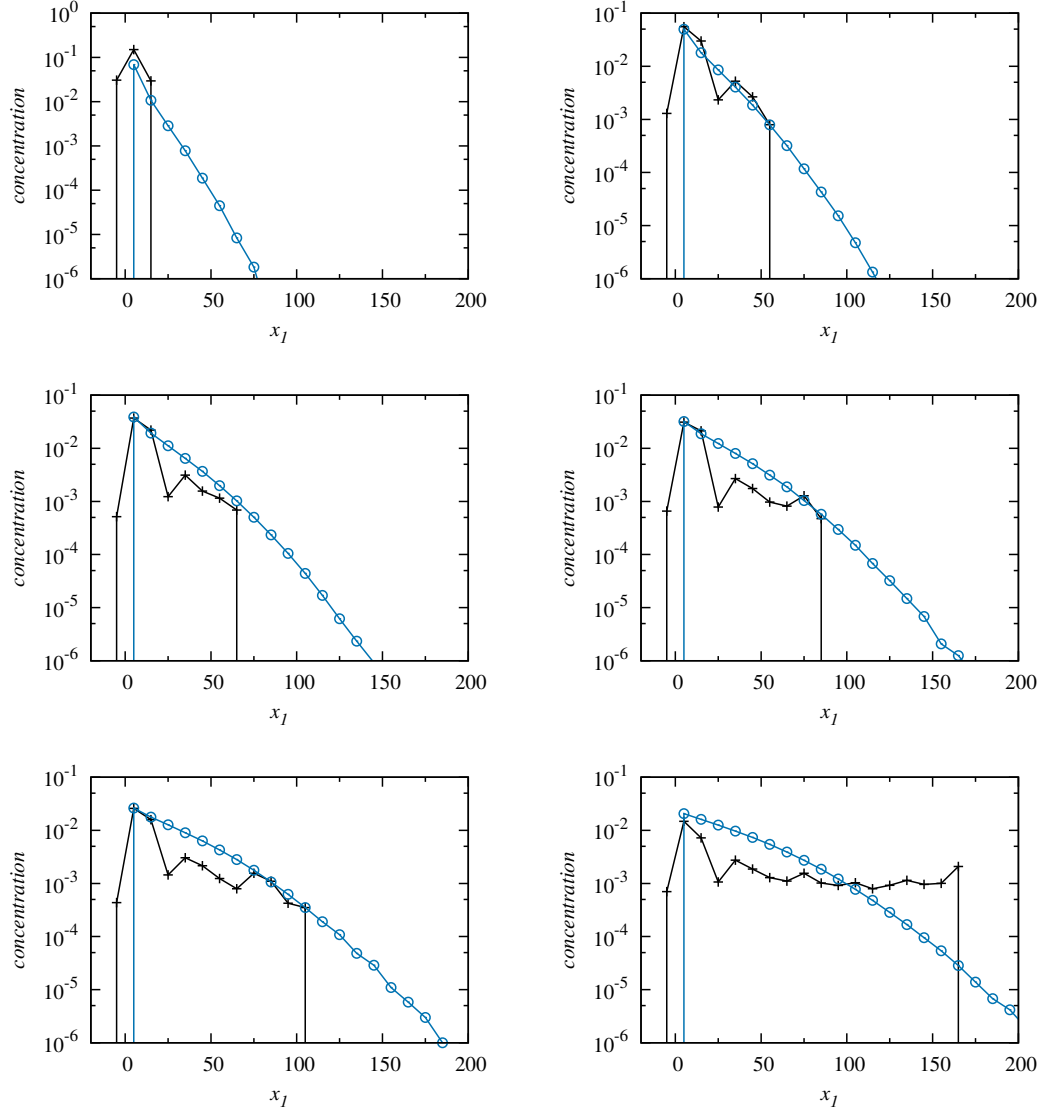
Figure 7. Same concentration data as in 2 plotted logarithmically on the concentration axis.

$K_g = 6.7 \times 10^{-6}$ m/s and the values at the upper and lower limits of the 95% confidence interval, $K_g = 10^{-5}$ m/s and $K_g = 4.3 \times 10^{-6}$ m/s, as well as the corresponding distributions of $\nu = \ln(v)$. The former underestimates the observed maximum concentrations because, as shown in the right panel of Figure 9 the distribution of ν is characterized by higher values than for the lower K_g. This feature together with the persistence represented by the correlation length ℓ_c of particle velocities leads to a relatively fast tracer release from the injection domain compared to the other values for K_g. The value of $K_g = 4.3 \times 10^{-6}$ m/s overestimates the maximum concentration because of strong tracer retention at the injection region due to low initial speeds. Nevertheless, as shown in Figure 8, both cases display qualitatively the same non-Gaussian behavior for the tracer profiles as the ones in Figure 2. This shows the robustness of the salient non-Gaussian transport features. This observation implies that the conductivity heterogeneity may be inferred from the evolution of the maximum concentration in the injection area.
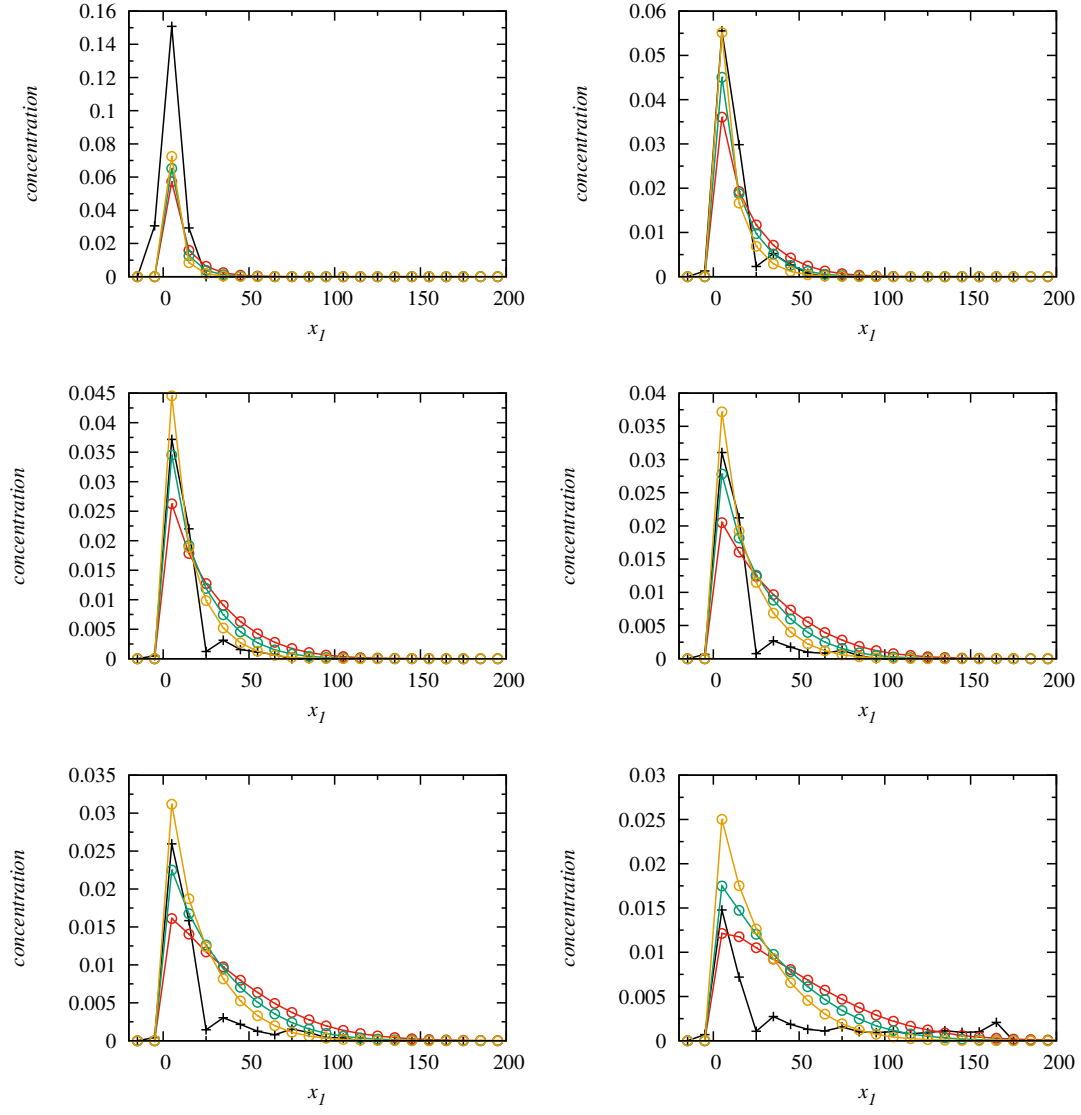
Figure 8. Concentration profiles from the (black crosses) MADE data and the upscaled model for an averaging window of (blue triangles) $\Delta x = 10$ m at times (top left to bottom right) $t = 49$ d, 126 d, 202 d, 279 d, 370 d and 503 d using a pointlike initial distribution. The values for the geometric mean conductivity are (orange) $K_g = 4.3 \times 10^{-6}$ m/s, (green) $K_g = 6.7 \times 10^{-6}$ m/s and (red) $K_g = 10^{-5}$ m/s
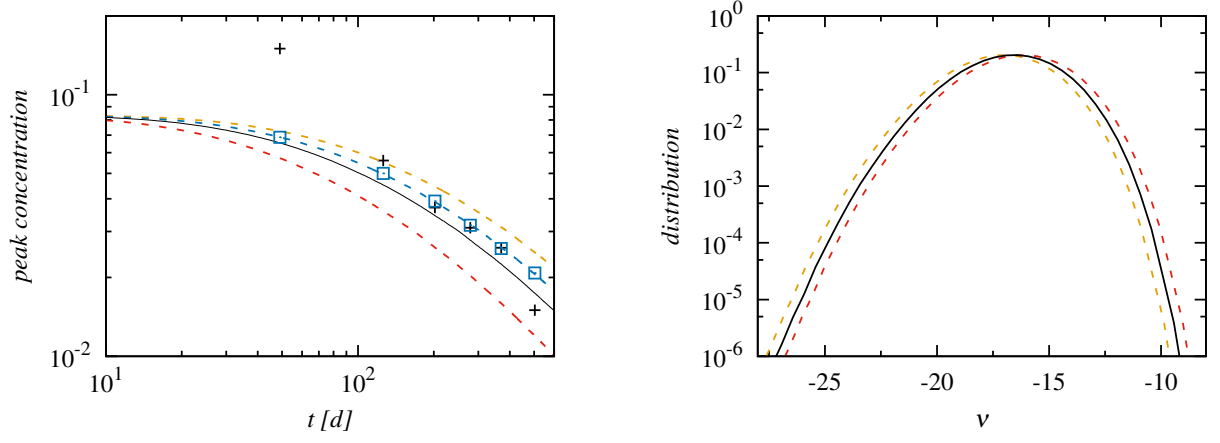
Figure 9. (Left panel) Maximum concentrations versus time from the (black crosses) MADE-1 data, and (blue squares) the prediction from the upscaled model with $\Delta x = 10$ m. The dashed lines denotes cumulative distribution of residence times (E1) obtained from the upscaled model for (orange) $K_g = 4.3 \times 10^{-6}$ m/s, (red) $K_g = 10^{-5}$ m/s. The thin black line denotes the prediction for $K_g = 6.7 \times 10^{-6}$ m/s. (Right panel) Distributions of the corresponding $\nu = \ln(v)$.